ADVANCED MATERIALS

Supporting Information

for *Adv. Mater.*, DOI: 10.1002/adma.201804097

Interfacial Defect Vibrations Enhance Thermal Transport in Amorphous Multilayers with Ultrahigh Thermal Boundary Conductance

Ashutosh Giri, Sean W. King, William A. Lanford, Antonio B. Mei, Devin Merrill, Liyi Li, Ron Oviedo, John Richards, David H. Olson, Jeffrey L. Braun, John T. Gaskins, Freddy Deangelis, Asegun Henry, and Patrick E. Hopkins**

Supporting Information

Interfacial Defect Vibrations Enhance Thermal Transport in Amorphous Multilayers with Ultrahigh Thermal Boundary Conductance

Ashutosh Giri, Sean W. King, William A. Lanford, Antonio B. Mei, Devin Merrill, Liyi Li, Ron Oviedo, John Richards, David H. Olson, Jeffrey L. Braun, John T. Gaskins, Freddy Deangelis, Asegun Henry, and Patrick E. Hopkins**

I. SAMPLE CHARACTERIZATION

Mono- and multi-layers of the SiC:H (with mass density, ρ=2.5 g cm^{-3}) and SiOC:H (ρ =1.6 g cm^{-3}) dielectrics were deposited on 300 mm diameter Si (001) substrates via plasma enhanced chemical vapor deposition (PECVD) the details of which have been previously provided.[1,2] Briefly, a commercially available PECVD system and tetramethylsilane diluted in hydrogen or carbon dioxide were utilized to deposit at 400 ℃ the SiC:H and SiOC:H films, respectively.

XRR spectra were collected using a Bruker D8 Discover (Cu ka). The data was collected in the range of 0 to 9000-15000 arcseconds with approximately 20 arcsecond steps.[3] Spectra were acquired and fitted using the Matlab software package. Along with XRR, the thickness of the films, multilayers, and individual laminates were also determined by XSEM measurements performed using an FEI Helios Nanolab scanning electron microscope at magnifications of 20-100,000X.[4] Note, the XRR and XSEM data confirm the periodic arrangement of SiOC:H/SiC:H layers, with period thicknesses ranging from ~3.4 to 26.4 nm.

Transmission FTIR spectra were collected from the SiC:H and SiOC:H films and multilayers using a Thermo Scientific Nicolet 6700 FTIR spectrometer and deuterated L-alanine doped triglycine sulfate (DLaTGS) detector. The spectra were acquired from 400-7000 cm^{-1} with 4 cm^{-1} resolution and signal averaged over 256 scans. Absorption from the silicon substrate was removed by scanning an uncoated silicon substrate and subtracting this spectrum from that for the film (or multilayer)/substrate spectrum. Thin film-substrate optical interference effects were removed using rigorous methods that accounted for the full wave nature of light and have been previously described in detail.[5-7]

Figure S1 shows characteristic XRR patterns for the various multilayer samples with and with-out plasma treatment. The XRR results show that for multilayers without the plasma treatment (including the thinnest period sample as shown in Figure S1d) the peak in the XRR pattern demonstrates superlattice reflections, which confirm the layered structures for these samples. However, for the samples with the N_2 plasma treatment between the layers, the XRR pattern for the thinnest period multilayer (see Figure S1e) does not show clear superlattice reflections.

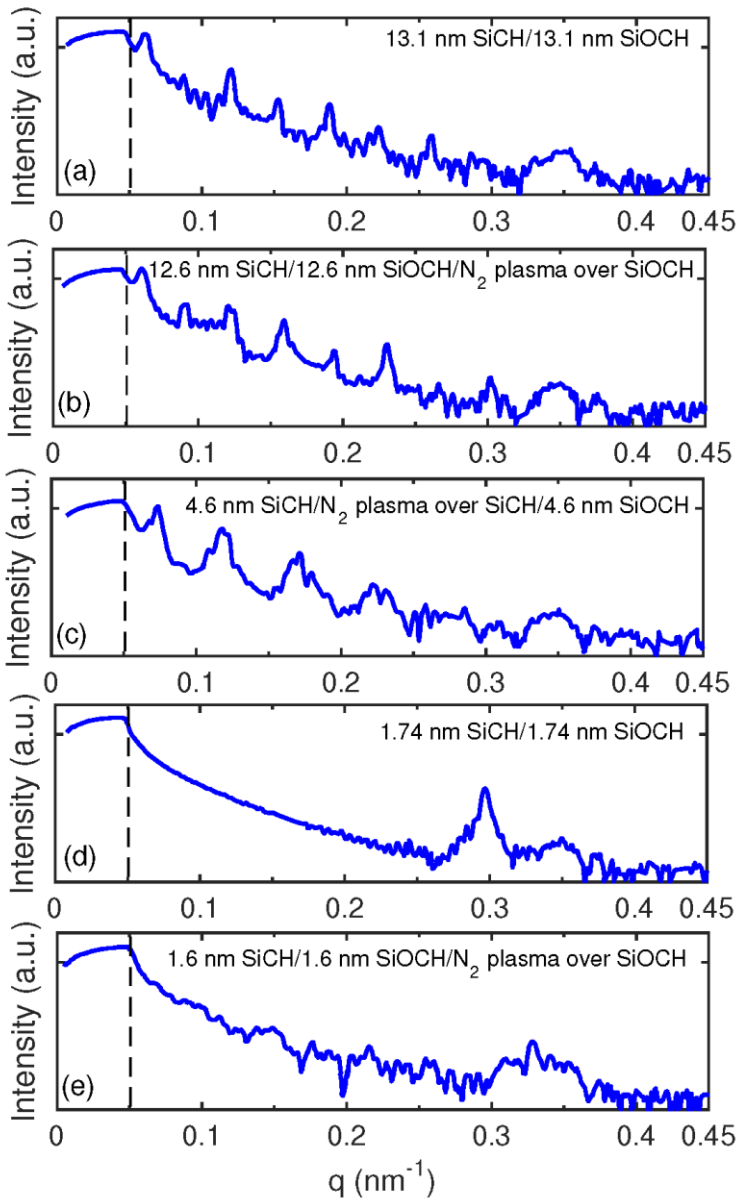

Figure S1. Characteristic XRR patterns for various period thickness multilayers with and without N_2 plasma treatment either on the SiOC:H or the SiC:H layer. For all period thicknesses except for the thinnest one with the N_2 plasma treatment on the SiOC:H layer, the XRR patterns for the multilayers show superlattice reflections.

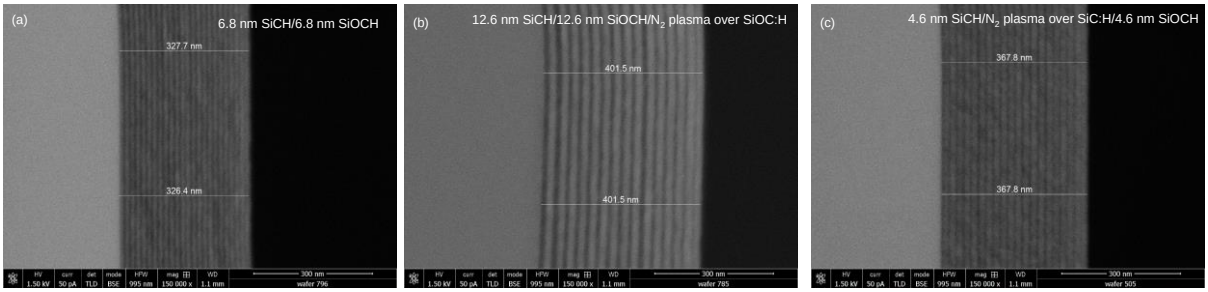

Figure S2. XSEM results showing film thickness as well as periodicity for various period thickness samples.

We use XSEM instead of our XRR measurements to determine the exact film thicknesses as the films are thicker than the XRR measurement limit. Characteristic XSEM images for a 6.8 nm SiC:H/6.8 nm SiOC:H, 12.6 nm SiC:H/12.6 nm SiOC:H/N_2 plasma over SiOC:H, and 4.6 nm SiC:H/N_2 plasma over SiC:H/4.6 nm SiOC:H are shown in Figures S1a S1b and S1c, respectively. The exact knowledge of film thicknesses for these multilayers is paramount for reducing uncertainty in their measured thermal conductivities as detailed below. However, the uncertainty introduced through the XRR measurements are negligible compared to the uncertainty from the aluminum transducer film thickness.

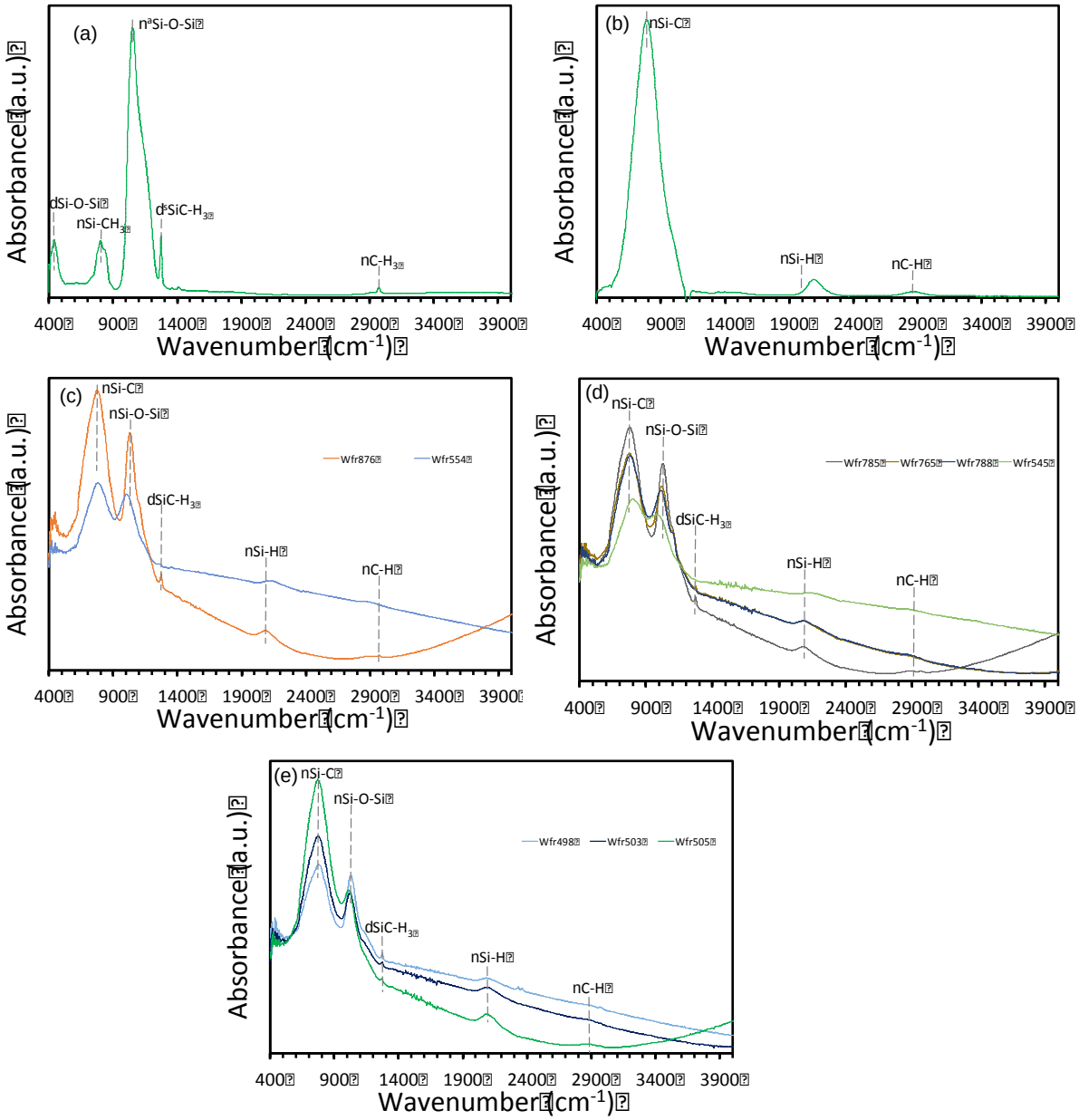

Figure S3. FTIR spectra showing characteristic bands for amorphous (a) SiOC:H, (b) SiC:H, (c) SiOC:H/SiC:H multilayers, (d) SiOC:H/N_2/SiC:H and (e) SiOC:H/SiC:H/N_2 multilayers.

Figure S3 shows a series of different FTIR spectra with the major absorption bands labeled. Mostly, these represent stretching bands for Si-H, C-H, N-H, Si-C, and Si-O bonds. The latter two of the bond stretching represent the main network bonding modes. There are also some rocking and deformation modes that are associated with the CH_3 groups (as labelled in the figure). The spectra for the multilayer samples are a composite overlay of the spectra for the

individual laminates, however, for the samples with the N_2 plasma treatment, the spectra are very different compared to that of the individual laminates. For the case where we ran the N_2 plasma on top of the SiOC:H, we clearly see the appearance of an N-H stretching mode at 3350 cm^{-1}. An Si-O/N related stretching band also appears at 900 cm^{-1}. This corresponds with a decrease in absorbance for the Si-O-Si stretching mode, SiC-H_3 deformation mode, and C-H stretching mode. All together, this indicates that the N_2 plasma is knocking out some of the terminal CH_3 groups in the SiOC:H dielectric and being replaced by N that further cross links the film.

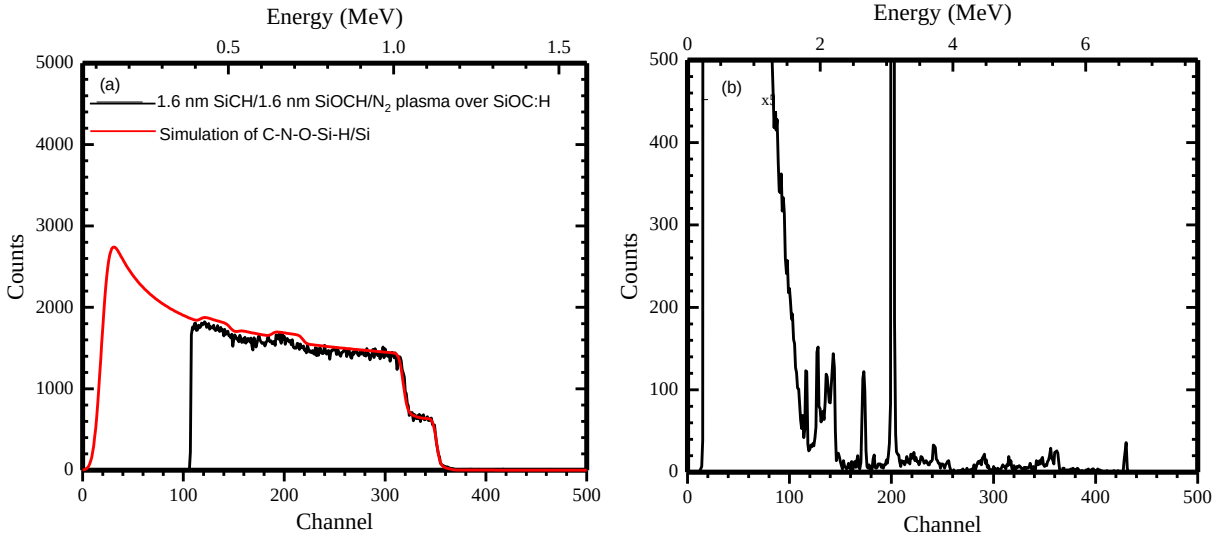

Figure S4. (Left column) 2 MeV RBS spectra with RUMP simulations based on composition given in Table S1. (Right column) Deuteron NRA spectra. Nuclear reactions peaks used in the analysis were as follows: $^{12}C(d,p_0)$, $^{14}N(d, \alpha_1)$, $^{16}O(d,p_0)^{17}O$, in channels ~202 , ~430, and ~180, respectively. All NRA spectra were recorded using a 2.4 MeV D_2+ beam with dose of 5 microcoulombs.

The H analysis was done using the 15N nuclear reaction method.[8] Briefly, this method makes use of a resonant nuclear reaction between 15N and H in the target. By measuring the number of characteristic gamma-ray from this reaction vs. beam energy, the H concentration vs depth in the target is determined.

The C, N and O contents were determined using deuteron nuclear reactions. The samples were bombarded with a deuteron beam at 1.2 MeV. Nuclear reactions occur between the deuterons and light elements in the film, giving peaks corresponding to $^{12}C(d,p_0)$, $^{14}N(d,\alpha_1)$, $^{16}O(d,p_0)$, in channels ~202 , ~430, and ~180, respectively. For sufficiently thin films, the counts in these peaks are proportional to the number of atoms/cm^2 of the respective isotopes. 2 MeV RBS was used to determine the Si content. Given the film composition for C, N, O, and Si the 15N NRA data were used to determine the H content in the film, also in units of 1015 atoms/cm^2. Once the complete composition of each film was determined as outlined above, the composition data were input to the Rutherford backscattering spectrometry (RBS) code RUMP to predict (with no free parameters) the complete RBS spectrum. This RUMP simulation was then compared to the data.

Table S1. Compositions (in percentage) and densities (ρ) of the samples measured via RBS and thicknesses for all the samples measured via XSEM. Thermal conductivities (κ) of the samples measured via TDTR and their respective Young's modulus (E) measured via nanoindentation are also tabulated.

Sample (wafer)	d (nm)	%C	%N	%O	%Si	%H	ρ(g cm^{-3})	κ(W m^{-1} K^{-1})	E(GPa)
SiOC:H (767)	1426	15.5 %	0.04 %	34.0 %	20.3 %	30.2 %	1.6	0.75	19.9±0.5
SiC:H (708)	828	37.1 %	0.00 %	0.3 %	36.3 %	26.3 %	2.5	1.50	204.5±7.2
13.2 nm SiC:H/13.2nm SiOC:H (876)	422	27.9 %	0.23 %	13.2 %	27.6 %	31.1 %	2.1	0.98	39.4±1.3
6.8 nm SiC:H/6.8 nm SiOC:H (796)	327	27.6 %	0.15 %	13.6 %	27.5 %	31.1 %	2.2	0.82	48.0±1.7
4.25 nm SiC:H/4.25 nm SiOC:H (780)	340	28.6 %	0.15 %	14.9 %	27.8 %	28.7 %	2.1	0.85	66.5±2.4
1.74 nm SiC:H/1.74 nm SiOC:H (554)	208.8	26.8 %	0.69 %	14.9 %	28.0 %	29.6 %	2.2	0.70	103.3±3.4
12.6 nm SiC:H/12.6 nm SiOC:H/N_2 (785)	403	27.0 %	0.81 %	14.1 %	28.9 %	29.2 %	2.2	0.95	45.7±1.6
6.5 nm SiC:H/6.5 nm SiOC:H/N_2 (765)	312	26.5 %	2.00 %	14.0 %	29.8 %	27.7 %	2.2	1.10	79.3±3.4
3.9 nm SiC:H/3.9 nm SiOC:H/N_2 (788)	311	27.0 %	2.80 %	13.6 %	28.9 %	27.7 %	2.2	1.10	98.8±2.8
1.6 nm SiC:H/1.6 nm SiOC:H/N_2 (545)	312	22.0 %	6.80 %	14.3 %	28.3 %	28.6 %	2.4	1.01	136.3±3.3
13.7 nm SiC:H/N_2/13.7 nm SiOC:H (498)	218.6	25.0%	1.80 %	14.9 %	26.9 %	31.6 %	2.2	0.96	33.9±1.9
10.4 nm SiC:H/N_2/10.4 nm SiOC:H (503)	249.6	26.5 %	2.00 %	14.0 %	29.8 %	27.7 %	2.3	1.13	66.1±3.9
4.6nm SiC:H/N_2/4.6 nm SiOC:H (505)	367.8	27.0 %	2.80 %	13.6 %	28.9 %	27.7 %	2.2	1.03	99.2±2.2
7.4 nm SiC:H/N_2 (672)	236	33.6 %	2.60 %	0.0 %	35.6 %	28.2 %	2.5	1.37	196.4±4.3
3.65 nm SiC:H/N_2 (331)	175	31.6 %	5.10 %	0.0 %	34.7 %	28.6 %	2.5	1.33	186.9±9.6
2.16 nm SiC:H/N_2 (182)	173	29.5 %	8.30 %	0.0 %	33.9 %	28.3 %	2.5	1.40	202.4±7.6
0.76 nm SiC:H/N_2 (180)	184	18.25 %	21.10 %	0.0 %	27.4 %	33.2 %	2.6	1.37	182.9±8.0
6.9 nm SiOC:H/N_2 (652)	222	13.5 %	1.60 %	37.9 %	21.7 %	25.3 %	2.1	0.67	38.91±2.6
2.5 nm SiOC:H/N_2 (345)	122	10.7 %	3.70 %	40.3 %	23.9 %	21.4 %	2.3	0.66	56.1±4.4
1.25 nm SiOC:H/N_2 (664)	100	7.1 %	4.60 %	37.7 %	23.2 %	27.4 %	2.5	0.77	75.8±8.3
0.71 nm SiOC:H/N_2 (751)	85	2.3 %	13.10 %	48.1 %	26.7 %	9.8 %	2.4	1.29	116.5±5.8

The evidence of nitrogen bonding states at the surface of the N_2 plasma treated films is an important aspect to be considered in this work, which requires in situ XPS measurements during the N_2 plasma treatments and is beyond the scope of the current work. However, *in situ* XPS spectra on similar SiOC:H films, which determines the surface chemical composition and provides evidence of nitrogen at the surface of SiOC:H films, have been reported in a prior work from one of the co-authors (in Ref. [9]). In that work, the *in situ* XPS measurements indicate that a surface amide layer containing N-C=O bonds is generated during exposure to N_2, which has a peak at 287.7 eV. Furthermore, the nitrogen core level at 399 eV indicative of C-N bonding was also observed, which provides further evidence of nitrogen bonding states at the surface of the plasma treated films.[9] Note, the use of the N_2 plasma treatments mostly stems from a practical stand point as the plasma treatments are utilized to improve adhesion of the SiC:H layer to Cu and SiOC:H to SiC:H.[9-11] Furthermore, the plasma treatment has also been shown to improve the electrical performance by reducing the leakage current density.[12] Along these lines, the increase in the concentration of carbon at the interface might be interesting from a comparative and theoretical perspective, the electrical performance of the device would be compromised given that it introduces trap states in the electronic band gap and would make the interface electrically leaky which is undesirable for microelectronic products.[13]

II. TIME DOMAIN THERMOREFLECTANCE MEASUREMENTS

Prior to the thermal measurements, we deposit ~80 nm of Al transducer layer, the thickness of which is measured via picosecond acoustics.[14] We measure the thermal properties of these samples via TDTR, the details of the technique and the analysis procedure are given elsewhere.[15-17] Along with the theoretical fits, Figure S5 shows TDTR data for our homogeneous SiOC:H and SiC:H samples as well as for a multilayer with ~3.48 nm period thickness. Note, we define the period length, L, as the sum of the thicknesses of each of the two individual layers; the interface density is then defined as $N = 2/L$. To accurately determine the thermal conductivities of the SiOC:H/SiC:H SLs, the heat capacities of the constituent layers in the SL must be determined first. Along with the thermal conductivities of the SLs, to accurately determine the intrinsic resistance at a single SiOC:H/SiC:H interface, the thermal conductivities of the individual layers are also required (as described in detail below). For this purpose, the thermal conductivities and heat capacities of the thickness series of homogeneous a-SiOC:H and a-SiC:H films are determined with a similar approach as implemented in our earlier work in Ref. [18]. In this approach, different pump-modulation frequencies are utilized to simultaneously measure the thermal conductivities and heat capacities of SiC:H and SiOC:H thin films. Figures S6a and S6b show the sensitivities of the ratio to the thermophysical parameters in the thermal model for a ~88 nm thick SiC:H film at 2 and 10 MHz pump-modulation frequencies, respectively. The most sensitive parameters in the model are the heat capacity and the thermal conductivity of the thin film. However, for a particular frequency, a range of heat capacities can produce the best-fit to the experimental data as shown in the contour plot of the residual error (see Fig. S6c). The common heat capacity and thermal conductivity values that produce the best-fit to the data for the two frequencies are taken as the measured values for the homogeneous samples. Using this approach, we measure thermal conductivity values of 1.48±0.12 W m^{-1} K^{-1} and 0.75±0.06 W m^{-1} K^{-1} and volumetric heat capacities of 1.9±0.3 J cm^{-3} K^{-1} and 1.3±0.2 J cm^{-3} K^{-1} for a-SiC:H and a-SiOC:H, respectively.

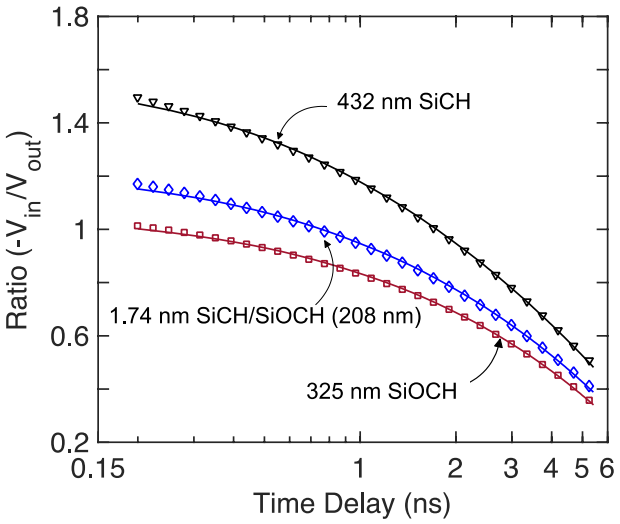

Figure S5. Sample data and best-fit curves for the 432 nm SiC:H (black triangles) and 325 nm SiOC:H (red squares) at a sample temperature of 300 K. For comparison, the TDTR data for a multilayer with 3.48 nm period thickness is also shown.

Initially, we fit the time domain thermoreflectance (TDTR) data for our homogeneous SiOC:H and SiC:H samples with a model that accounts for thermal diffusion in a 3 layer system by fitting for thermal boundary conductances across the Al/film and simultaneously fitting for the thermal conductivity of the films. All other parameters in our thermal model such as the thermal conductivities and heat capacities of the transducer and substrate layers are taken from literature[20]; note, due to small thermal resistance of Al/film or film/Si interfaces, we are negligibly sensitive to these thermal boundary conductances as we discuss below.

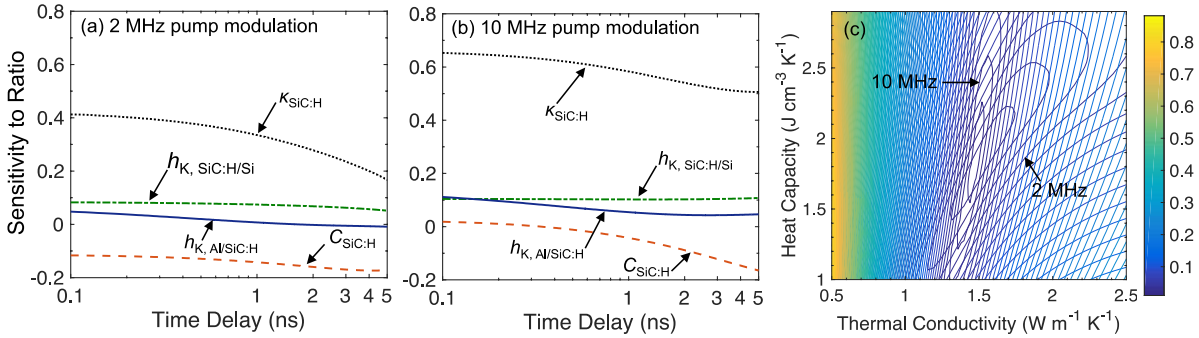

Figure S6. Sensitivities of ratio ($-V_{\text{in}}/V_{\text{out}}$) to the thermo-physical properties of a 88 nm thick SiC:H sample as a function of pump-probe time delay at (a) 2 MHz pump modulation frequency and (b) 10 MHz pump modulation frequency. (c) Sensitivity contour plot showing the interrelationship between thermal conductivity and heat capacity of a 88 nm SiC:H sample at 2 MHz and 10 MHz pump modulation frequencies.

To evaluate the thermophysical properties of interest in our control samples, namely the heat capacity and thermal conductivity of our samples, we must determine the appropriate range of pump-probe delay time to fit the thermal model to the experimental data, in which the thermal model is extremely sensitive to changes in these parameters[17,21]. The sensitivity of the ratio to various thermal properties is defined by,

$$S_x = \frac{\partial \ln(-V_{\text{in}}/V_{\text{out}})}{\partial \ln(x)} \qquad (1)$$

where x is the thermophysical parameter of interest and V_{in} and V_{out} are the in- and out-of-phase signals, respectively. Figures S6a and b show the sensitivities of the ratio to the thermophysical parameters in the thermal model for a ~88 nm thick SiC:H film at 2 and 10 MHz pump-modulation frequencies, respectively. The most sensitive parameters in the model are the heat capacity and the thermal conductivity of the thin film. However, for a particular frequency, a range of heat capacities can produce the best-fit to the experimental data as shown in the contour plot of the residual error (Figure S6c). The common heat capacity and thermal conductivity values that produce the best-fit to the data for the two frequencies are taken as the measured values for the homogeneous samples. Using this approach, we measure thermal conductivity values of 1.48±0.12 W m^{-1} K^{-1} and 0.75±0.06 W m^{-1} K^{-1} and volumetric heat capacities of 1.9±0.3 J cm^{-3} K^{-1} and 1.3±0.2 J cm^{-3} K^{-1} for SiC:H and SiOC:H, respectively.

Figure S7 shows the measured thermal conductivity of the SiOC:H and SiC:H films as a function of film thickness as determined via the approach detailed above. In contrast to a-Si where considerable size effects dominate the thickness dependent thermal conductivity, the thermal

conductivities our amorphous SiOC:H and SiC:H films with different film thicknesses are constant within experimental uncertainties as shown in Figure S7.

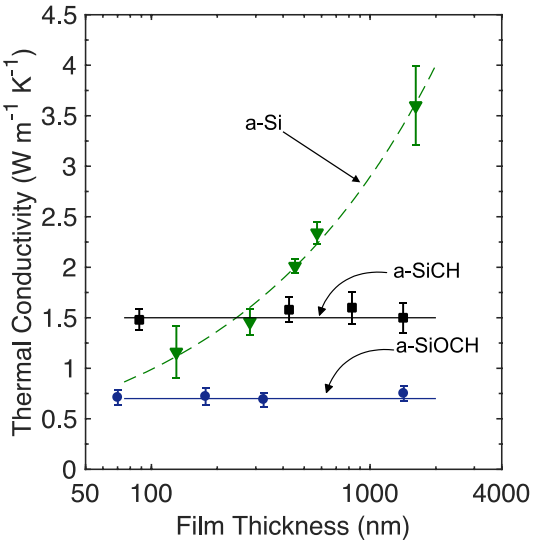

Figure S7. Thermal conductivity of a-SiC:H and a-SiOC:H films as a function of film thickness. The lack of size effects for both amorphous structures suggest that thermal transport is mostly mediated by diffusons. Also included are the measured thermal conductivities of amorphous Si from Ref. [19] that show considerable size effects due to the contribution from propagating modes to the thermal conductivity.

III. MOLECULAR DYNAMICS SIMULATIONS AND LATTICE DYNAMICS CALCULATIONS

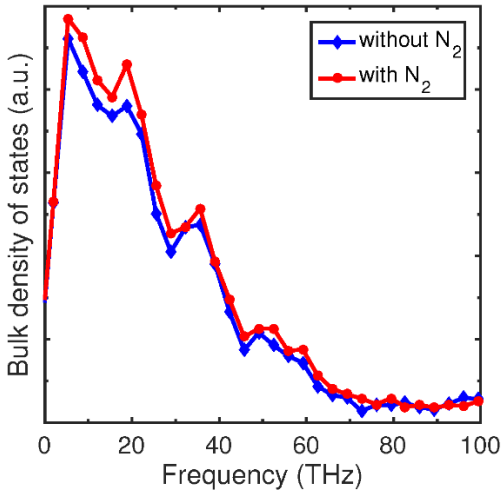

Figure S8. Bulk density of states predicted by a super cell lattice dynamics (SCLD) calculation for a short 2.5 nm period 2.5 nm period SiC:H/SiOC:H multilayer structure with and without nitrogen defects at the interface.

Figure S8 shows the bulk DOS calculated for the SiOC:H/SiC:H structures with and without N_2 within ±7 Å of the interfaces. These are predicted by a super cell lattice dynamics (SCLD) calculation for a short 2.5 nm period multilayer structure and the interatomic potential is defined by the ReaxFF potential that is widely used to model hydrocarbon interactions.[22] To construct the supercells a method was used that places atoms randomly in space and

converges to the pair distribution function. The pair distribution functions for amorphous silicon carbide were used as a starting point to build the SiC:H structures, where the Si, C and H concentrations were 37.2 %, 36.4 %, and 26.4 %, respectively. These structures were constructed to match the density measured in experiments and consisted of 8000 atoms. Once these base structures were constructed, oxycarbide structures were made by randomly substituting atoms in the SiC:H structure for oxygen atoms and relaxing the structures through a series of annealing steps involving repeated/sequential molecular dynamics (MD) runs using isobaric and isothermal constraints until the potential energy remained constant. Once obtained, the superlattice structures were built by taking supercells of each material, joining them at the interface and annealing again using the same procedure, until the potential energy remained constant. Once the superlattice structures were constructed, the versions with N_2 added near the interface were built using the same method, but this time leaving a space between the SiC:H and SiOC:H structures that was populated with nitrogen atoms. Once added, the structures were again extensively annealed until the potential energy became constant. Using this supercell preparation procedure, we then relaxed the structures, by performing MD simulations with velocity rescaling, where the temperature was continually rescaled to absolute zero. In this way the atoms gradually reached their equilibrium positions, which then allowed for SCLD calculations, yielding the DOS and all normal mode information. The modes were then segregated into the categories identified by Gordiz and Henry, and the DOS specific to the interfacial modes is given in the main text. The bulk DOS as shown in Figure S8 for these structures are very similar, which suggests that the introduction of Nitrogen defects at the interface does not significantly alter the DOS of these multilayers. We note that the correlation and coupling between the interfacial modes and the bulk modes could potentially lead to a stronger understanding of the microscopic heat transfer in these AMLs. However, to fully gauge the effect of coupling of the two sets of modes with and with-out the presence of nitrogen at the interface on the thermal transport across these materials, a full interface conductance modal analysis (ICMA)[23] calculation needs to be performed, which is beyond the scope of the current work. As such, we leave the ICMA analysis as future theoretical work to understand the coupling between the various modes and their effect on the overall heat transfer and thermal conductivity of these materials.

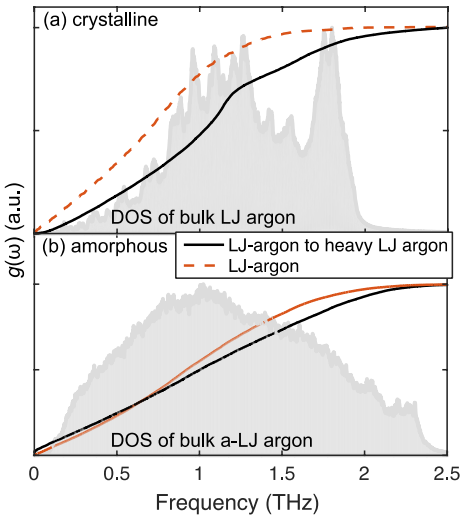

Figure S9. Normalized spectral contributions to heat flux across the bulk of crystalline LJ-Ar and contributions to the heat flux from LJ-Ar to a mass heavy LJ-Ar. (b) Normalized spectral contributions to the corresponding amorphous phases.

To emphasize the difference in the spectral heat flux across crystalline and amorphous interfaces instead of investigating material specific properties, we also simulate solids defined by the generic 6-12 Lennard-Jones (LJ) potential. Therefore, to better understand the effect of amorphicity on interfacial resistance, we compare the contributions of different vibrational frequencies at LJ-based amorphous/amorphous and crystalline/crystalline interfaces by calculating the spectral contributions to the heat flux from a Solid A to Solid B (as detailed in our earlier work in Ref. [24]).

Figure S9a shows the spectral contributions to the heat flux in the bulk of crystalline LJ argon (solid line) and the spectral contributions due to the heat flux impinging on mass heavy argon ($4m_{\mathrm{Ar}}$) from the argon side (in a system domain with argon/mass-heavy argon as detailed in Ref. [24]). Similarly, Fig. S9b shows the spectral contributions to heat flow across the corresponding amorphous phases. The figures also include the local DOS for the crystalline and amorphous phases. The DOS for the amorphous solid has a broader spectrum with almost similar DOS in the spectrum of frequencies, whereas, for crystalline LJ argon, the frequency range in middle of the spectrum has the higher DOS. This is replicated by the spectral contributions to the heat flux in the bulk of crystalline argon being concentrated more in the middle range of frequencies in the spectrum, while for the amorphous phase, heat is almost equally carried by the broad range of frequencies in the entire spectrum. This shows that the heat carrying vibrations are very different between the amorphous and crystalline phases. For an amorphous/amorphous interface, the better overlap between the heat carrying vibrations on either side of the interface (even though the acoustic mismatch between the layers is large) results in the lower interfacial resistance as compared to interfaces that are comprised of highly dissimilar crystalline materials.

References

[1] S. King, M. French, J. Bielefeld, W. Lanford, *J. Non-Cryst. Sol.* **2011**, *357*, 2970.

[2] X. Guo, H. Zheng, S. W. King, V. V. Afanas'ev, M. R. Baklanov, J.-F. de Marneffe, Y. Nishi, J. L. Shohet, *Appl. Phys. Lett.* **2015**, *107*, 082903.

[3] S. W. King, D. Jacob, D. Vanleuven, B. Colvin, J. Kelly, M. French, J. Bielefeld, D. Dutta, M. Liu, D. Gidley, *ECS J. Solid State Sci. Technol* **2012**, *1*, N115.

[4] V. Miikkulainen, O. Nilsen, H. Li, S. W. King, M. Laitinen, T. Sajavaara, H. Fjellvag, *J. Vac. Sci. Technol., A* **2015**, 33, 01A101.

[5] M. Milosevic, S. W. King, *J. Appl. Phys.* **2012**, 112, 093514.

[6] S. W. King, M. Milosevic, *J. Appl. Phys.* **2012**, *111*, 073109.

[7] G. Stan, R. S. Gates, Q. Hu, K. Kjoller, C. Prater, K. J. Singh, E. Mays, S. W. King, *Beilstein J. Nanotechnol*. **2017**, *8*, 863.

[8] W. Lanford, M. Parenti, B. Nordell, M. Paquette, A. Caruso, M. Mantymaki, J. Hamalainen, M. Ritala, K. Klepper, V. Miikkulainen, O. Nilsen, W. Tenhaeff, N. Dudney, D. Koh, S. Banerjee, E. Mays, J. Bielefeld, S. King, *Nucl. Instrum. Methods B* **2016**, *371*, 211.

[9] X. Liu, S. Gill, F. Tang, S. King, R. Nemanich, *J. Vac Sci. Technol. B* **2012**, *30*, 031212.

[10] K. Ueno, V. M. Donnelly, Y. Tsuchiya, *J. Vac Sci. Technol. B* **1998,** *16*, 2986.

[11] H.-C. Tsai, Y.-S. Chang, S.-Y. Chang, *Microelectron. Eng.* **2008**, *85(7)*, 1658.

[12] Y. -W. Li, C.-F. Chen, *Japanese J. Appl. Phys.* **2002**, *41*, 5734.

[13] M. J. Mutch, T. Pomorski, B. C. Bittel, C. J. Cochrane, P. M. Lenahan, X. Liu, R. J. Nemanich, J. Brockman, M. French, M. Kuhn, B. French, S. W. King, *Microelectron. Reliab.* **2016**, *63*, 20.

[14] C. Thomsen, H. T. Grahn, H. J. Maris, J. Tauc, *Phys. Rev. B* **1986**, *34*, 4129.

[15] D. G. Cahill, *Rev. Sci. Instrum.* **2004**, *75*, 5119.

[16] A. J. Schmidt, X. Chen, G. Chen, *Rev. Sci. Instru.* **2008**, *79*, 114902.

[17] P. E. Hopkins, J. R. Serrano, L. M. Phinney, S. P. Kearney, T. W. Grasser, C. T. Harris, *J. Heat Transfer* **2010**, *132*, 081302.

[18] A. Giri, J.-P. Niemelä, C. J. Szwejkowski, M. Karppinen, P. E. Hopkins, *Phys. Rev. B* **2016**, *93*, 024201.

[19] J. L. Braun, C. H. Baker, A. Giri, M. Elahi, K. Artyushkova, T. E. Beechem, P. M. Norris, Z. C. Leseman, J. T. Gaskins, P. E. Hopkins, *Phys. Rev. B* **2016**, *93*, 140201.

[20] C. Y. Ho, R. W. Powell, P. E. Liley, *J. Phys. Chem. Ref. Data* **1972**, *1*, 279–422.

[21] R. M. Costescu, M. A. Wall, D. G. Cahill, *Phys. Rev. B* **2003**, *67*, 054302.

[22] A. C. T. van Duin, S. Dasgupta, F. Lorant, W. A. Goddard, *J. Phys. Chem. A* **2001**, *105*, 9396.

[23] K. Gordiz, A. Henry, *J. Appl. Phys.* **2016**, *119*, 015101.

[24] A. Giri, J. L. Braun, P. E. Hopkins, *J. Phys. Chem. C* **2016**, *120*, 24847.